ACS APPLIED MATERIALS & INTERFACES

RESEARCH ARTICLE

www.acsami.org

Thermally Induced Transformations of Amorphous Carbon Nanostructures Fabricated by Electron Beam Induced Deposition

Dhaval D. Kulkarni, Konrad Rykaczewski, Srikanth Singamaneni, Songkil Kim, Andrei G. Fedorov, and Vladimir V. Tsukruk*

School of Material Science and Engineering and Woodruff School of Mechanical Engineering, Georgia Institute of Technology, Atlanta, Georgia 30332-0245, United States

ABSTRACT: We studied the thermally induced phase transformations of electron-beam-induced deposited (EBID) amorphous carbon nanostructures by correlating the changes in its morphology with internal microstructure by using combined atomic force microscopy (AFM) and high resolution confocal Raman microscopy. These carbon deposits can be used to create heterogeneous junctions in electronic devices commonly known as carbon−metal interconnects. We compared two basic shapes of EBID deposits: dots/pillars with widths from 50 to 600 nm and heights from 50 to 500 nm and lines with variable heights from 10 to 150 nm but having a constant length of 6 μm. We observed that during thermal annealing, the nanoscale amorphous deposits go through multistage transformation including dehydration and stress-relaxation around 150 °C, dehydrogenation within 150−300 °C, followed by graphitization (>350 °C) and formation of nanocrystalline, highly densified graphitic deposits around 450 °C. The later stage of transformation occurs well below commonly observed graphitization for bulk carbon (600−800 °C). It was observed that the shape of the deposits contribute significantly to the phase transformations. We suggested that this difference is controlled by different contributions from interfacial footprints area. Moreover, the rate of graphitization was different for deposits of different shapes with the lines showing a much stronger dependence of its structure on the density than the dots.

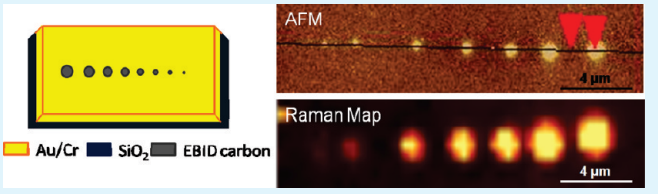

KEYWORDS: amorphous and nanocrystalline carbon, electron-beam-induced deposition, graphitization

INTRODUCTION

Carbon deposits with tunable conductivities are important for many prospective electronic applications. As known, carbon can exist in different forms owing to its tendency to undergo three different types of hybridizations; sp^1, sp^2, and sp^3.[1] A wide range of electronic properties ranging from insulating/semiconducting to metal-like (graphite, nanotubes and graphene) can be tuned by adjusting the sp^3/sp^2 content and nanostructure morphologies of carbon materials. Amorphous carbon is a metastable form of carbon which shows the presence of both sp^2 and sp^3 carbon bonds. Its high chemical stability, optical transparency and excellent mechanical properties make it important in areas of protective coatings and optoelectronics.[2−5] On the other hand, phase transformation of these amorphous carbon deposits into highly conductive localized graphitic structures opens a wide opportunity for their use in electronic devices.

Several fabrication techniques can be used for the deposition of carbon in the form of ultrathin coatings and individual nanostructures. These methods include chemical vapor deposition,[6] cathodic arc deposition,[7] pulsed laser deposition[8] and sputtering.[9] Depending on the deposition methods and settings, amorphous carbon films with different microstructures and sp^2/sp^3 contents have been produced.[10−12] The characterization of these microstructures basically involves determining the atomic order and chemical composition as the sp^3/sp^2 ratio. Different techniques such as diffraction, NMR, X-ray reflectivity, electron energy loss spectroscopy and Raman spectroscopy have been used for obtaining these parameters. Most of these techniques were used to study the properties of bulk amorphous carbon films deposited on a substrate.[11,13−16]

Raman spectroscopy is one of the most important tools for characterizing the microstructure of various carbon materials (graphite, amorphous carbon, carbon nanotubes, graphene), primarily because of its nondestructive approach, presence of sharp peaks, and high intensity of these characteristic peaks. This technique provides a wide range of critical information for bulk carbon materials, nanoscale structures, carbon-based nanocomposites, and individual carbon structures, including the composition, internal stresses, and crystal orientation inside the material.[17−20]

All amorphous and graphitic carbon structures have been known to show characteristic peaks for D band and G band near 1350 cm^{-1} and 1580 cm^{-1}, respectively. Raman spectra of carbon structures is greatly dominated by the sp^2 sites because of their 50−230 times larger Raman scattering cross-section than the sp^3 sites.[21] Thus, the Raman spectra of tetrahedral amorphous carbon which contains only 10−15% sp^2 content is still dominated by the presence of the characteristic peaks. G-mode is

Received: October 20, 2010
Accepted: January 24, 2011
Published: February 14, 2011

associated with the stretching vibrations of any pair of sp^2 sites, whether in C=C chains or in aromatic rings. The D-mode is the breathing mode of those sp^2 sites located only in rings but not in chains.[12,15,22]

In recent study, Tuinstra and Koenig reported that the intensity ratio of the D and G peaks varies inversely with the in-plane correlation length, La or grain size of the graphite.[23] In another fundamental work, Ferrari et al. found that it is possible to classify the transformation of carbon microstructure as deduced from Raman spectra of all disordered carbons within a three-stage model of increasing disorder starting from perfect graphite, as follows: (1) transformation of graphite to nanocrystalline graphite; (2) transformation of nanocrystalline graphite to sp^2 amorphous carbon with presence of aromatic rings; (3) further transformation of mostly sp^2 amorphous carbon to completely disordered sp^3 amorphous carbon with fragmented and chain configurations. In these transformations, stage 1 corresponds to the progressive reduction in the grain size of ordered graphite layers, while keeping the aromatic rings. Second, stage 2 corresponds to the topological disordering of a graphite layer (odd membered rings) and loss of aromatic bonding, but with a purely sp^2 network. In stage 3, the sp^3 content increases from 0 to 100%. This changes the sp^2 configuration from mainly rings to short chains.[22,24] These changes in the microstructure are also associated with the changes in the density of the substrate. Finally, amorphous carbon which is insulator is reported to show a density between 1.8 and 2.1 g/cm^3, whereas graphite with high electrical conductivity has a density of 2.3 g/cm^3, thus resulting in a 15% decrease in specific volume.[25,26] Complete graphitization and formation of nanocrystalline graphite is usually observed at temperatures above 600 °C.

Recently, electron-beam-induced deposition (EBID) has been shown to be a useful tool for localized (nanoscale) deposition of amorphous carbon and metals with complex 2D/3D geometry over different substrates. At room temperature, organic molecules present on the substrate have sufficient mobility to migrate and become a precursor for deposition reaction. A precursor molecule, when it interacts with an electron of appropriate energy (i.e., secondary electrons generated upon impact of electron beam on a substrate), dissociates and results in the formation of an immobile carbon deposit.[27−29] As has been demonstrated, electron beam in conventional SEM can be used for the growth of such carbon deposits.

These EBID deposits can be used as soldering material to improve the contact of heterogeneous materials at the interface (e.g., metal−metal or metal−semiconductor interface).[30] In addition to this, it can be deposited over a relatively small area (<1000 nm^2), which makes it important for nanoscale patterning of surfaces and in electronic circuits, where localized fusion of the metal joints is required.[31−33] But, as deposited, the EBID carbon is amorphous and has low electrical conductivity, thus limiting its use in electronic circuits as materials for interconnets.[34] Thus, postdeposition treatment, including microstructure modification (dehydrogenation and residual stress relaxation) and directed phase transformation (i.e., toward much higher electrically conductive graphitic phase) is required after EBID process.[35]

Several methods have been proposed to lower the electrical resistance of the amorphous carbon via graphitization. Thermal annealing has been widely used for graphitization of amorphous carbon films. On subjecting a carbon film to high temperature, several processes can take place. Studies on thermal annealing of thin amorphous carbon films have shown that significant structural changes occur around 400 °C followed by completed graphitization at 600−800 °C.[36−42] However, no studies have been reported on the microstructure and morphology of the amorphous EBID carbon deposits having nanoscale dimensions (well below a micrometer scale) where the role of the interfaces become dominant and thermal behavior can be much different from that observed for bulk carbon materials.

Here, we demonstrate that dramatic and complex thermally induced changes in chemical and physical states of EBID carbon nanostructures can be revealed by using a combination of atomic force microscopy (AFM) and confocal Raman microscopy techniques. EBID carbon deposits in the form of one-dimensional (lines) and zero-dimensional (dots) having characteristic dimensions within 50−500 nm were analyzed for their changes in microstructure with annealing temperature up to 500 °C. The size of the deposits was also varied to account for the effect of confinement on the process of phase transition. The change in the density of the deposits upon change in the microstructure was analyzed by recording the changes in their shape by using AFM. Concurrently, confocal Raman measurements were performed on the same individual carbon deposits with lateral resolution of 300 nm.[43]

Correlating the Raman data with the AFM measurements revealed multistage transformations of the amorphous carbon deposits, well-known for bulk carbon materials but at much lower annealing temperatures. Complete graphitization along with formation of densified nanocrystalline carbon structures was achieved at temperatures around 400 °C, which is much lower than that for bulk amorphous carbon. Both dots and lines undergo similar thermally induced transformations but more significant transitions are observed for carbon lines because of their higher structural dependency on the density ($height^2 \approx 1/density$) than the dots ($height^3 \approx 1/density$).

RESULTS AND DISCUSSIONS

EBID Deposits Fabrication. The carbon deposits were grown over a 50 nm layer of gold layer deposited on 10 nm layer of chrome over a silicon oxide layer on a silicon substrate as shown in Scheme 1. EBID deposits are known to be hydrogenated amorphous carbon containing more sp^2 than sp^3 bonded carbon.[33] Electron beam focused at a spot for prolonged period of time lead to the formation of "dot" like structures from residual hydrocarbons ("contamination") as a precursor, as shown in Figure 1a. SEM images of deposits upon tilting the substrate at 45° with respect to the electron beam, reveal a pillar like morphology of these deposits (Figure 1b). These deposits were obtained by varying the e-beam current from 1.5 to 400 pA and accelerating voltage from 10 to 30 keV. Although, the electron beam exposure time was maintained constant for all deposits, their morphology showed a significant variation with EBID parameters. The widths of these nanostructures can be controlled in the range from 100 to 1000 nm and their heights can be varied from 50 nm to several micrometers (Figure 1b). The details of the carbon deposit morphology with the deposition settings are discussed elsewhere.[34]

The intrinsic physical state of these carbon deposits was confirmed from their characteristic Raman spectra collected from individual carbon structures with Raman micromapping under minimum laser power (Figure 2). The images were obtained by integrating the intensity of the peaks between

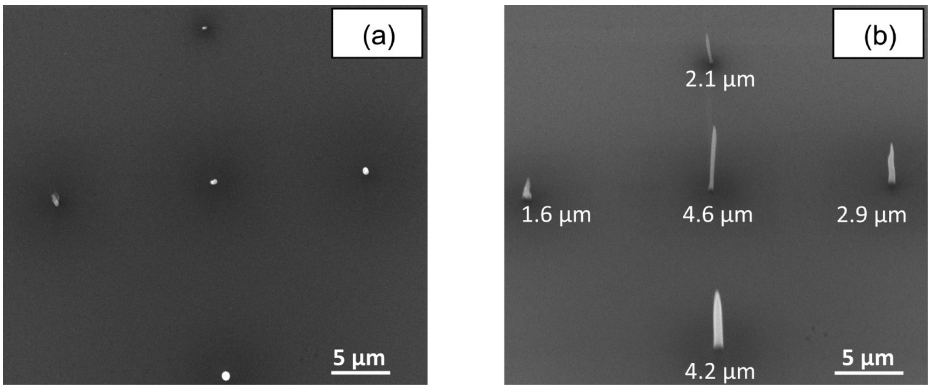

Figure 1. SEM images of EBID carbon dots deposited under different settings. (a) Top view of the deposits showing dot like structures; (b) 45° view of the deposits showing pillar like morphology with the values underneath indicating its height.

Scheme 1. Deposition Geometry of EBID Carbon Deposits Arrays with Different Shapes and Sizes of Dots and Lines Fabricated on Au/Cr Substrates

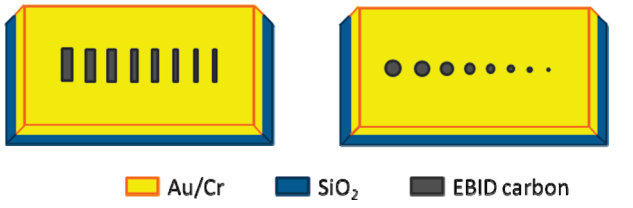

1000 cm^{-1} and 1800 cm^{-1} to account for the characteristic D- and G- peaks.[13] Thus, the deposits which show peaks in this range appear brighter as compared to other regions. Figure 2b shows the high-resolution Raman spectra in this selected range obtained from the corresponding deposits by averaging over 400 individual spectra. Though, the deposits show a different morphology (see Figure1b), their Raman spectra are virtually identical with the G band peak position varying between 1560 and 1565 cm^{-1} and D/G ratio around 1.3. Thus, although the deposits were fabricated under different electron beam conditions and showed different morphologies and dimensions, they had a similar composition and microstructure with significant sp^3 content suggesting the dominance of amorphous and highly fragmented carbon material.[1,22]

After evaluating the effect of e-beam deposition settings, carbon dots of different dimensions were grown by varying the exposure time at fixed e-beam parameters for detail studies. The electron beam parameters were kept constant by maintaining the e-beam current and accelerating voltage at 25 pA and 20 keV respectively, with the exposure time varying from 5 to 240 s. Figure 3 shows the AFM image of these carbon dots (Figure 3a) and cross-sectional profile (Figure 3b) with the corresponding 3D AFM image (Figure 3c).

A uniform gradient in the size of these deposits is observed with height and width of dots increasing, as the exposure time increases. The smallest dot with the height of 60 nm and width about 200 nm was obtained at an exposure time of 5 s with the largest dot having the height of 450 nm with width reaching 500 nm. To study the microstructure of these deposits, Raman maps were obtained as described before (Figure 3d). The measurements were made under minimum laser power (0.5 mW) to avoid any laser light induced thermal effects. The smallest deposits were practically invisible on Raman maps because of their very low signal-to-noise ratio and thus were excluded from further Raman spectral analysis (two smallest dots on left in Figure 3a).

Carbon deposits in the form of line with identical length and different cross-sections were grown by scanning the e-beam back and forth across the surface. The length of the line was kept constant by maintaining a constant scan area but its height was varied by changing the exposure time. Figure 4a shows the AFM of the lines having the same lengths but with increasing thickness/height from left to right. The thinnest line having the height and width of 2 and 70 nm, respectively, was obtained at an exposure time of 30 s. Sectional analysis (Figure 4b).shows a systematic increase in the height of these lines from left to right. Figure 4c displays a representative 3D image of the line with the height of the line varying along its length with the height gradually decreasing toward the center. This is due to a higher rate of diffusional supply of precursor molecules at the corners as compared to the edges and is common for EBID deposits.[29,33]

The array of carbon lines were also analyzed using Raman micromapping (Figure 4d). The smallest carbon line deposits (<10 nm) did not show up in the Raman image (similar to dots) and thus were excluded from further Raman spectral analysis (two thinnest lines on left in Figure 4a). The substrate with the line deposits was also annealed at same range of temperatures and analyzed for its morphology and microstructure at every step by AFM measurements and Raman spectroscopy under conditions identical to those applied to variable-size carbon dots.

Thermal Annealing of Carbon Deposits. *Morphological Changes.* AFM and Raman measurements were collected for exactly the same deposits for each thermal annealing cycle. Measurements were performed at each thermal annealing step by moving the substrate with microscopic location marks using a micromanipulator to exactly locate the same surface area for all the readings. Thus, all data points presented here, represent the same selected deposits, which go through all thermal transformations. One-time capturing of both AFM and Raman images for all carbon deposits annealed at given temperature minimize instrumentation variations related to differences in sample preparation, thermal treatment, and imaging, thus providing for the highest resolution and a solid base for comparative studies of these very small amounts of carbon deposits.

Figure 5 demonstrates the variation in height of the carbon deposits with different sizes (heights) annealed at different

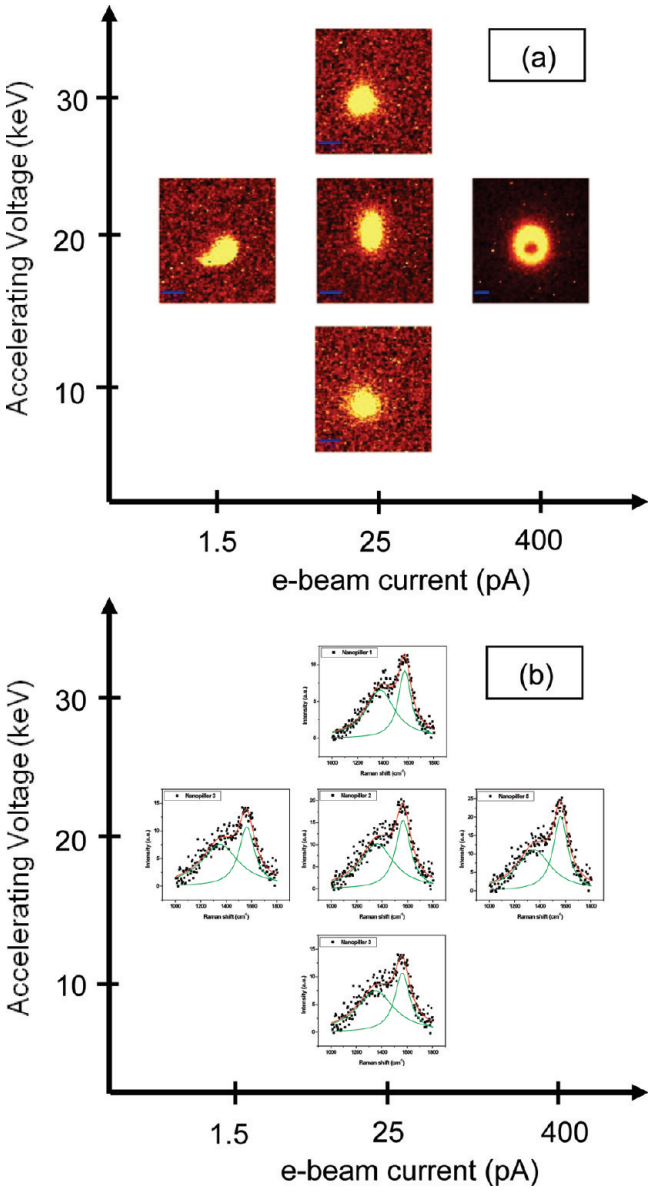

Figure 2. Raman micromapping of the carbon dots fabricated under different e-beam settings. (a) Raman maps (scale bar is 1 μm); (b) corresponding Raman spectra.

temperatures as measured from averaging multiple cross sections of AFM images. As clear from this data, all the carbon dots show a small decrease in their size with the increase in annealing temperature from 30 °C to 250−300 °C. However, some decrease in size is observed above 300 °C with a higher rate observed for smaller dots. On the contrary, carbon lines show a much more distinct change in their size on annealing at higher temperatures (Figure 5b). All the carbon lines show a steady decrease in height up to 300 °C followed by a sharp decrease, the most prominent (∼75%) being for the smallest line (60 nm). Modest structural changes (10−30%) were also observed for the lines with the smallest cross-section.

A similar trend is observed for the widths of these deposits annealed at different temperatures (Figure6). All the dots show a slight decrease in their widths with the increase in annealing temperature. It is interesting to note that the dots with relatively smaller widths (<200 nm) show a more pronounced decrease in their widths. However, a distinct transition is difficult to interpret from this data alone. On the contrary, lines show a gradual decrease in their widths on annealing from 30 to 300 °C followed by a step decrease around 450 °C. Interestingly, it was observed that the length of the line does not change with the annealing temperature. Thus, for simplification, all the discussions henceforth will focus on analyzing the variation in height of the deposits, keeping into consideration that the widths will follow a similar trend and the volume of deposits decreases with thermal annealing as well .

On analyzing the separate plots for carbon dots and lines with approximately similar cross sections, a significant change in the height (∼75%) was observed for smallest line as compared to a mere 20% decrease for smallest dot at the highest annealing temperatures (Figure 7). Smallest lines (<15 nm) were not visible at temperatures above 300 °C owing to greatly diminished dimensions because of densification and partial ablation.

Decreasing height of the carbon deposits suggests that they are undergoing significant densification during thermal annealing at elevated temperatures, which can be related to both graphitization and clustering of initially amorphous and porous carbon deposits. These trends indicate that the transformation process primarily depends on the cross-sectional area of the deposits. The most significant structural changes are observed for carbon deposits having feature size less than 100 nm. Intense transformation for the smallest deposits suggests that the reorganization process relies on the efficient transfer of thermal energy across the deposit which further implies that the metal (Au/Cr)−carbon

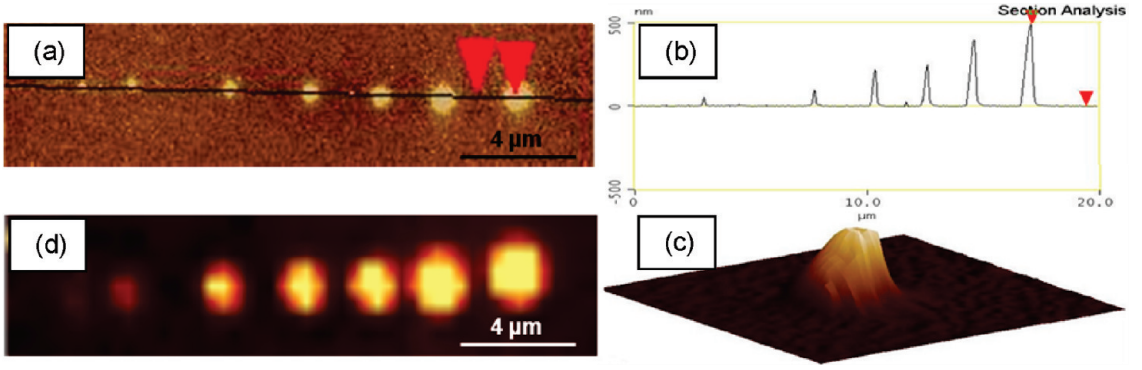

Figure 3. Linear array of EBID-fabricated carbon dots with different dimensions. (a) AFM image showing the section line; (b) cross-section; (c) representative 3D image (z-scale is 450 nm); (d) Raman map.

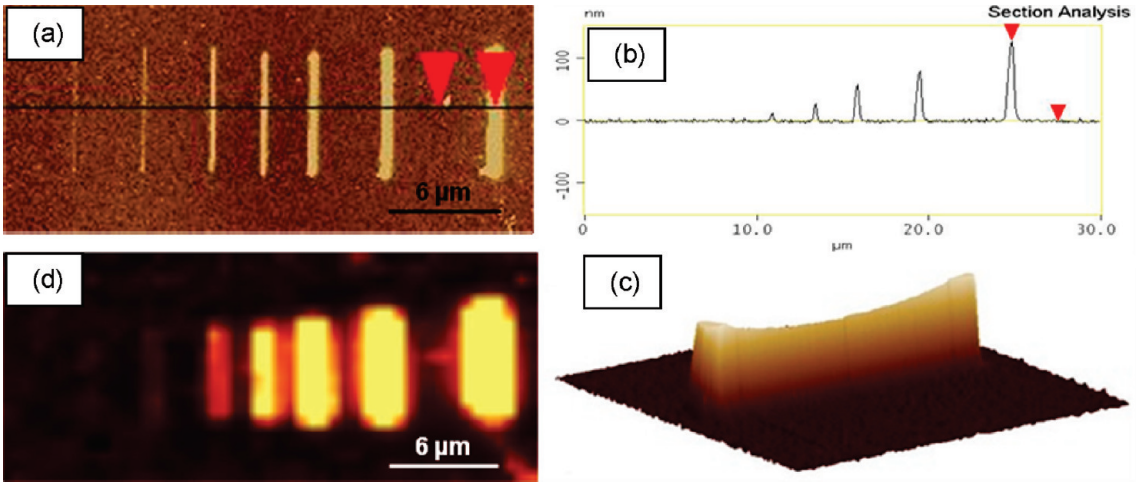

Figure 4. Linear array of EBID-fabricated carbon lines with different dimensions. (a) AFM image showing the section line; (b) cross-section; (c) representative 3D image (z-scale is 150 nm); (d) Raman map.

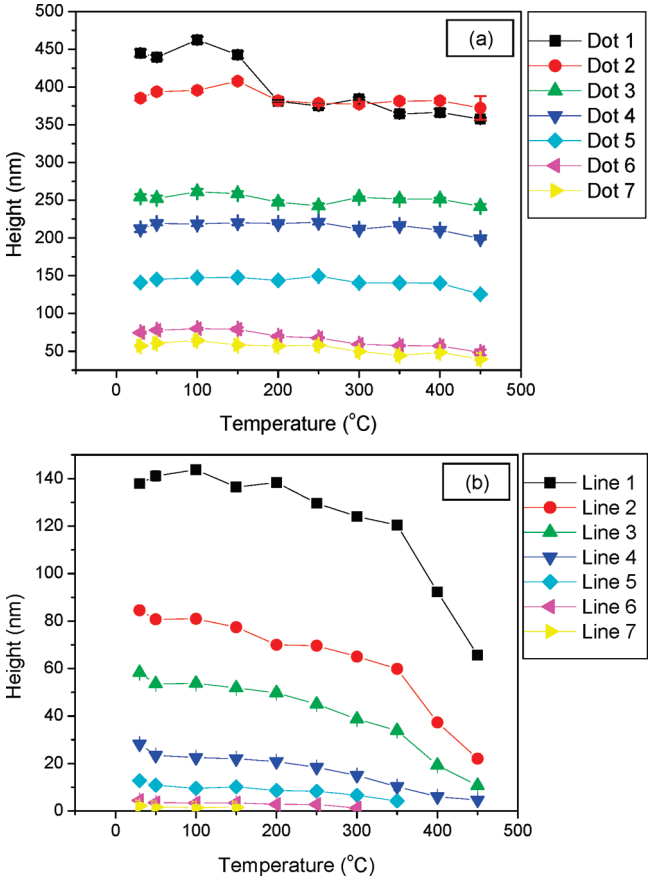

Figure 5. AFM height analysis of (a) carbon dots and (b) carbon lines at different annealing temperatures.

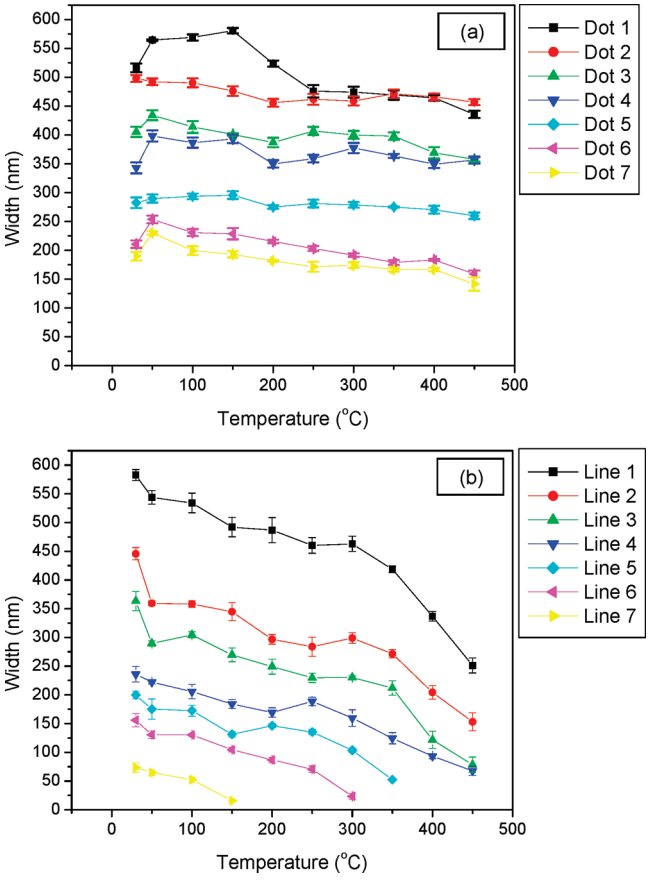

Figure 6. AFM width analysis of (a) carbon dots and (b) carbon lines at different annealing temperatures.

interface should have a significant contribution in this process. It is worth to note that the surface area of the substrate covered by the lines is much higher than that occupied by the dots. Comparing the deposits having the similar heights, it is seen that the line footprint covers a surface area of $2.9 \pm 1.0\ \mu m^2$ whereas the dot footprint cover just $0.047 \pm 0.025\ \mu m^2$. Even the bigger dots show an average footprint of $0.6 \pm 0.35\ \mu m^2$ which is much lower than that for the smallest line again.

In fact, the interface with metal substrate might act as a site for nucleation of the graphitic crystallites inside the amorphous carbon structure during extensive annealing as caused by thermally induced interfacial stresses between materials with different thermal properties. Thus, the first nucleation should occur at the low energy gold surface and at the interface of the carbon deposit. In case of the deposits with similar heights, the surface area per unit volume available for the nucleation is the same.

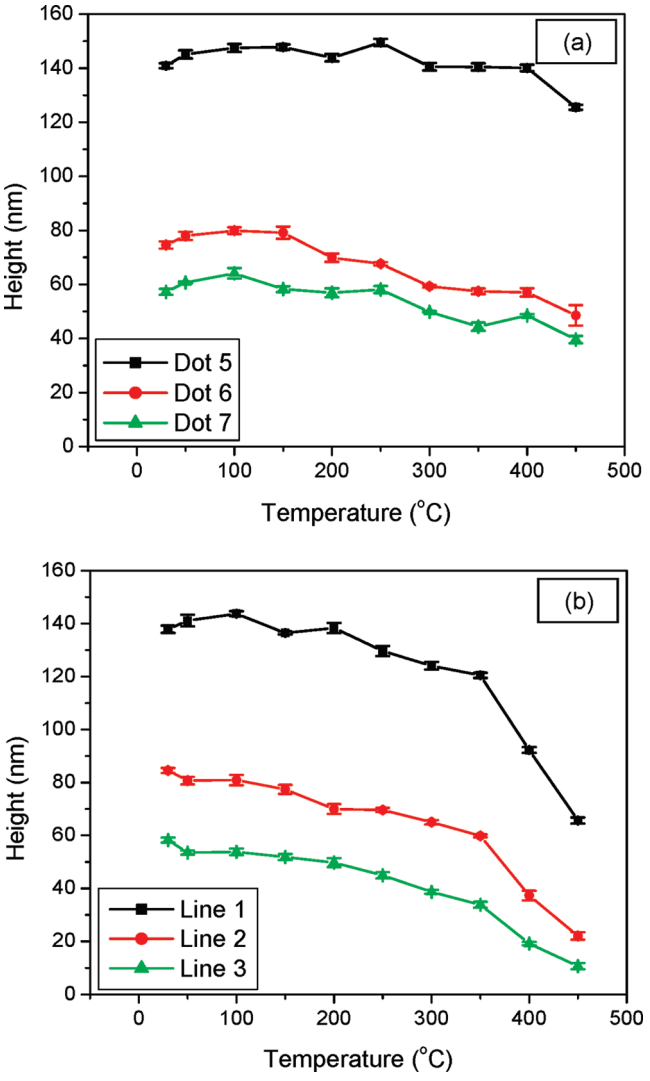

Figure 7. AFM height analysis of (a) carbon dots and (b) carbon lines having similar initial heights, at different annealing temperatures.

We suggest that at elevated temperatures, the formation of the interfacial layer of graphitic crystalline domains takes place inside the deposits. With the further increase in annealing temperature, the growth of the crystal domains takes place resulting in further densification of deposits. The rapid decrease in the height of the lines, implying a higher growth rate of crystalline domains is likely due to the height^2 $\approx$ 1/density or even height $\approx$ 1/density (for taller lines) dependence for lines simply because at least one dimension − the line length is largely fixed and the change of volume occurs due to a change in other dimensions.

For the dots, on the other hand, because all three dimensions are likely to shrink at approximately the same rate as the density increases upon graphitization, the height vs density dependence is much weaker: height^3 $\approx$ 1/density. Thus, a steady decrease in the height is observed for the lines with the increase in the annealing temperature. Apparently, much higher energy is required to drive the crystal growth inside the dots due to significant space constraints and small footprint as compared to carbon lines. Considering that further increase in annealing temperature leads to a dramatic reduction in size, which well-exceeds the expected densification caused by complete graphitization

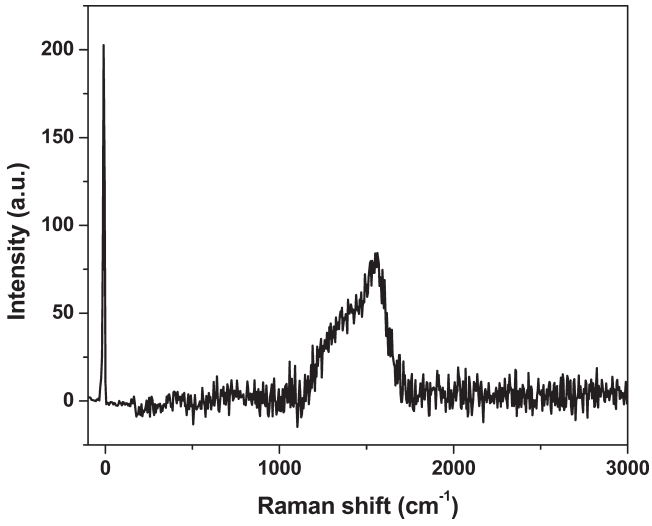

Figure 8. Representative integrated EBID Raman spectra of carbon deposits (carbon line) at room temperature.

(15%), the possibility of intense ablation of the lines could be suggested as well. To elucidate the actual nature of the chemical and physical transformation, the Raman spectra need to be carefully analyzed.

Raman Monitoring of Carbon Deposit Transformations. Figure 8 shows the representative Raman spectra of the carbon deposits (carbon line) at a single point, taken at room temperature which demonstrates all major features representing material under investigation: Broad peaks between 1300−1600 cm^{-1} represent the characteristic D band and G band peaks of carbon as introduced above. The extremely weak peak near 1050 cm^{-1} might be due to the vibration of monosubstituted benzene rings.[44] The height of the deposits (50−500 nm) is significantly smaller compared to the depth of focus (700 nm). Hence, the spectra obtained here accounts for the entire volume of the deposit, considering that focal plane coincides with the substrate. It should be noted that the spectra appears more noisy and without clearly defined shoulder owing to its collection from a single point on the carbon deposit (carbon line in this case), whereas all other spectra (discussed below) represents an average of several points over the deposit.

The two major characteristic peaks that correspond to D band and G bands are difficult to analyze in this representative spectrum, but they can be clearly observed and deconvoluted when zoomed in a narrower window between 1000 and 1800 cm^{-1} as apparent in Figure 9, which shows the evolution of the Raman spectra of a carbon line annealed at different temperatures. Similar trends can be observed for the spectra of carbon dots annealed at different temperatures. These spectra were utilized for further analysis after deconvoluting with the Lorentzian fits to clearly distinguish the characteristic G band and D band

As clear from Figure 9, the D band appears as a shoulder to the more intense G band at lower temperature. As the annealing temperature increases, the D band becomes more prominent in the spectra along with the increase in intensity of G band as well. Also, the full width at half-maximum (FWHM) of the G band was found to decrease by almost 35% (140 cm^{-1} to 90 cm^{-1}) as the annealing temperature increases. For further detailed analysis of the microstructure, we selected the positions of D and G bands as

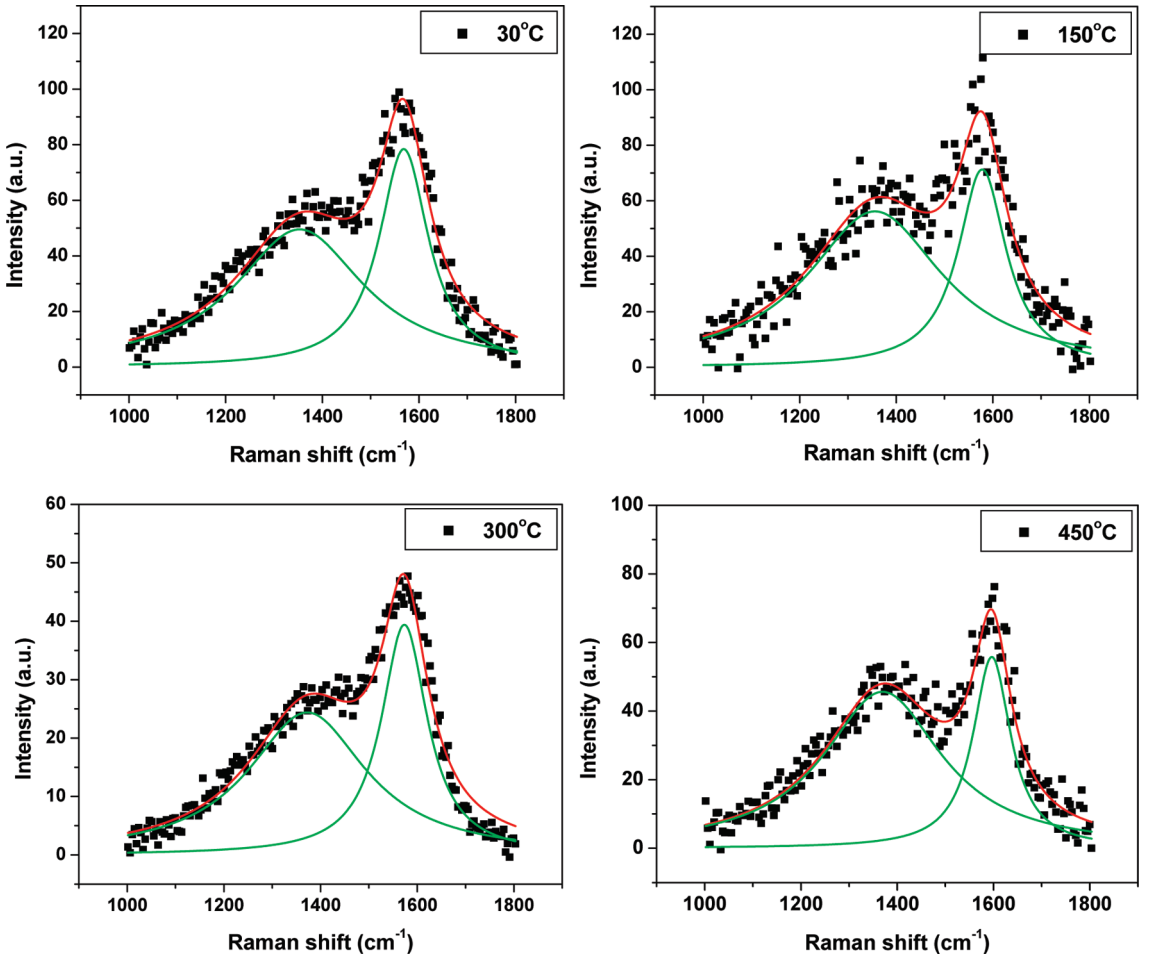

Figure 9. Evolution of Raman spectra for EBID carbon deposits (carbon line) at different temperatures.

well as the ratio of their peak areas as commonly referred in literature. As mentioned earlier, D band correspond to the breathing mode of sp^2 sites in rings and G band relates to the stretching vibration of any pair of sp^2 sites in chains or aromatic rings. In case of graphite, as the disorder increases, the cluster size and number decreases and gets more distorted until it opens up. Because the G peak is just related to the relative motion of C sp^2 atoms, the $I(G)$ increases with respect to $I(D)$ and the ratio decreases. On the contrary, in case of amorphous carbons having a small correlation length (L_a), the D mode stretch is proportional to the probability of finding a 6-fold ring in the cluster which in turn is proportional to the cluster area. Thus, in amorphous carbons, the development of a D peak indicates ordering, exactly opposite from the case of graphite.[22,23]

Figure 10 indicates that the D/G ratio undergoes significant variation with increasing annealing temperature, showing a gradually increase from 1.0 to 1.4 to 2.0−2.2 for both carbon dots and lines. Moreover, overall behavior for dots and lines is similar within standard deviations indicating that shrinking dimensions do not significantly affect the thermally induced phase transformations. Thus general trends will be analyzed after averaging for all dots and all lines with different sizes as represented by the solid black lines (averaging over all data points) in the subsequent figures. The smaller dots (<140 nm in height) and lines (<15 nm in height) were excluded from the averaging owing to their low signal-to-noise ratio. However, the data points are included in the figures for consistency.

D/G ratio has been known to be a quantitative factor in determining the size of graphitic crystallites in any carbon structure.[10] It is accepted that the increase in the D/G ratio corresponds to the increase in the correlation length of the graphitic crystallites. Ferrari et al. showed that the D/G ratio for amorphous carbon materials varies between 0 and 2.5: 0 being a characteristic of 100% amorphous structure and 2.5 corresponding to a more graphitic structure.[24] At room temperature, the D/G ratio for all the dots occurred between 1.2 and 1.4, suggesting a mixed sp^2 and sp^3 character typical for hydrogenated amorphous carbon (Figure 10a). As the annealing temperature increased, the D/G shows a 22% increase around 100 °C followed by a gradual decrease which extends to 300 °C. This change can be assigned to removal of adsorbed/absorbed moisture, dehydrogenation (annealing at ambient conditions) and stress-relaxations occurring inside the carbon structures deposited at metal surface.[45] At annealing temperatures between 100 and 300 °C, the Raman bands for dots show a 22% decrease in their D/G ratio. This implies the initiation of structural changes inside the dots. After reaching shallow minima at 300 °C, the D/G ratio shows a steep rise (36%), reaching around 2.5 at 450 °C. This sharp increase in the D/G ratio indicates the dramatic ordering of the graphitic domains and conversion into nanocrystalline graphitic material at the highest annealing temperature.

A similar variation in D/G ratio is observed for carbon lines annealed at different temperatures (Figure 10b). Indeed, the

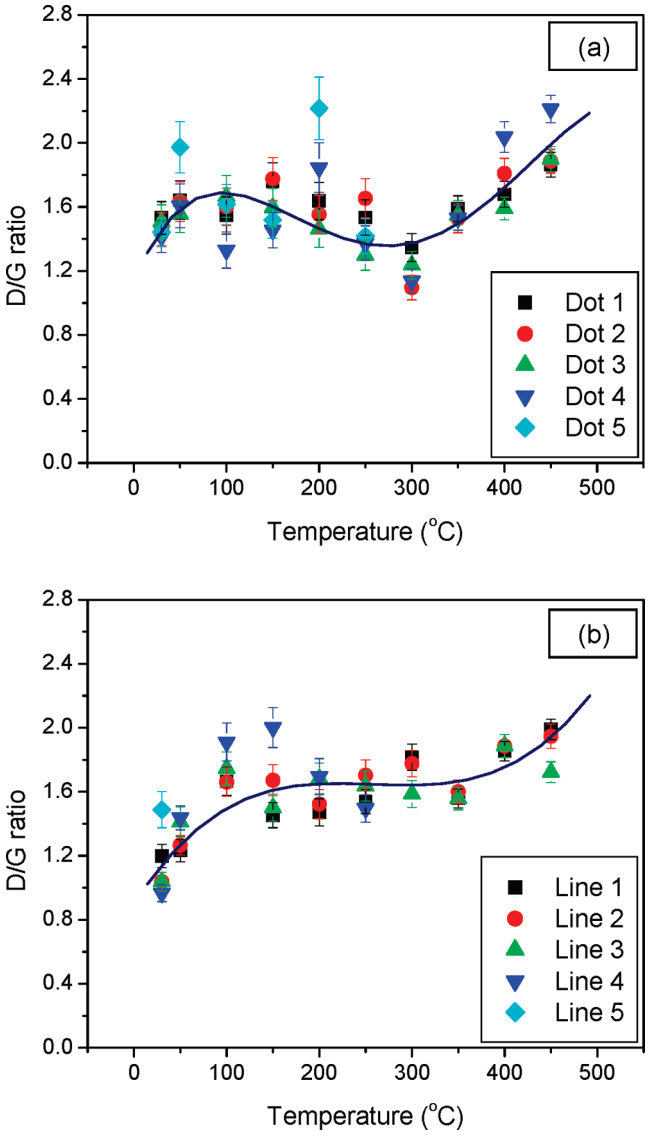

Figure 10. D/G ratio analysis of (a) carbon dots and (b) carbon lines at different annealing temperatures. Solid line represents the average of the data points for all sizes at given annealing temperature.

D/G ratio for lines at room temperature lies between 1.0 and 1.2, a little lower than the carbon dots. As temperature increased, the D/G ratio showed a steep increase (60%) for temperatures up to 150 °C corresponding to the process of moisture removal, dehydrogenation and stress relaxation similar to dots. The process is more prominent owing to the much pronounced structural response of the lines toward the heat transfer across the interface of the line as compared to the dots. This is also relates to the steady decrease in the dimensions of the lines witnessed from the AFM measurements. Further increasing the annealing temperature leads to no apparent changes in the D/G ratio up to 350 °C, suggesting the formation and clustering of the graphitic crystals inside the deposits without significant changes in composition and density. Above 350 °C, the D/G ratio showed a gradual increase up to 2.2 at 450 °C. This also corresponds to the temperature range at which lines show a dramatic decrease in their height. Thus, from the AFM and Raman measurements it appears that the carbon lines are fully graphitized and densified around 400 °C.

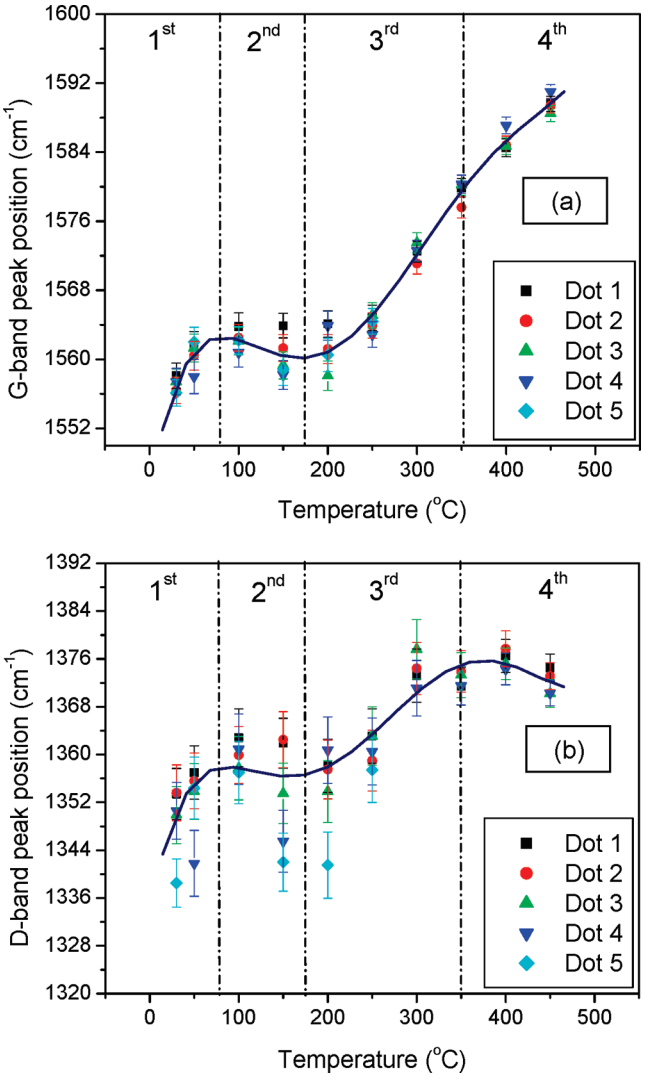

Figure 11. G band peak position (a) and D band peak position (b) for carbon dots annealed at different temperatures. Solid line represents the average of the data points for all sizes at given annealing temperature.

Although the dots show a similar trend in their Raman spectra variations, stress relaxation that occurs in carbon dots at intermediate annealing temperatures is completely absent in corresponding lines. This difference suggests that the long lines studied here are a subject of lower initial stresses related to the limited contribution from small volume of carbon in direct contact with the substrate.

To further elaborate the above suggestion made based upon densification dynamics and D/G ratio variation, we analyze the G and D band positions of the deposits annealed at different temperatures (Figures 11, 12). G band is known to have a strong dependence on the amount of the graphitic crystallites present in the carbon structure. It is known to vary from 1520 to 1600 cm^{-1} depending on the amount and ordering of the graphitic nanocrystallites. A red shift of the G band toward higher wavenumbers corresponds to the increase graphitization and ordering of nanocrystals.[22]

Figure 11a shows the variation of G band peak position for the carbon dots annealed at different temperatures. As deposited, the EBID dots show G band peak position around 1556 cm^{-1} at room temperature suggesting a significant presence of sp^3

dx.doi.org/10.1021/am1010173 |ACS Appl. Mater. Interfaces 2011, 3, 710–720

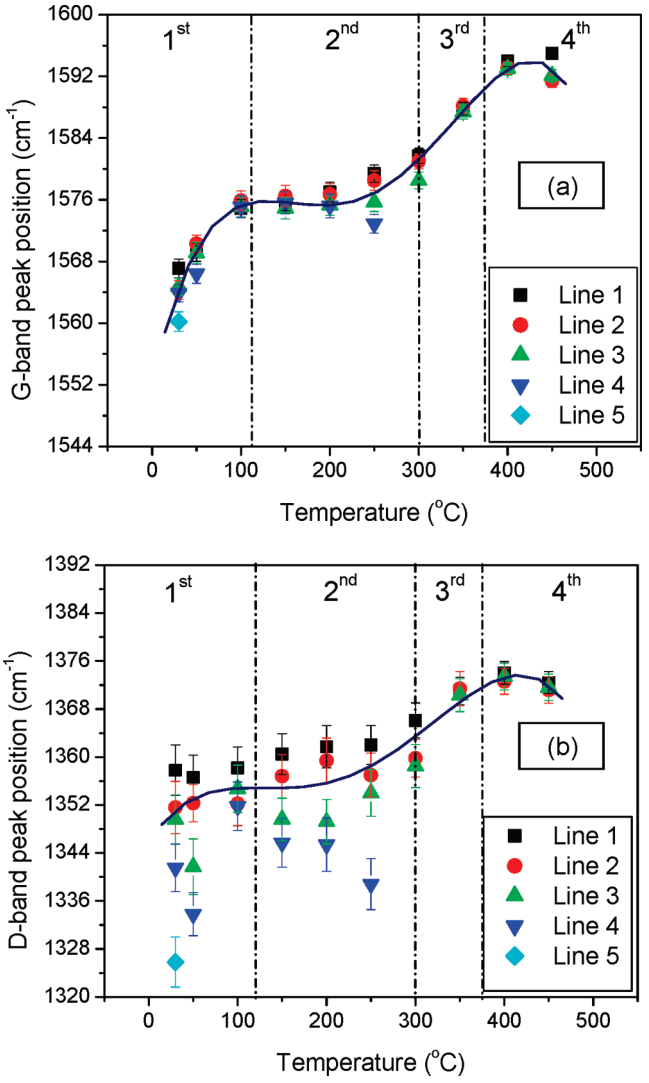

Figure 12. (a) G band peak position and (b) D band peak position for carbon lines annealed at different temperatures. Solid line represents the average of the data points for all sizes at given annealing temperature.

content in the system with disordered microstructure, a characteristic of amorphous carbon as was indicated above. As the annealing temperature increases up to 100 °C, the G band shows a shift toward higher wavenumbers, reaching 1560 cm^{-1} followed by a slight down shift and a further increase above 200 °C. At higher annealing temperatures, the G band position linearly increases to 1580 cm^{-1} (at 350 °C), which is related to the formation of ordered graphite nanostructures. With the further increase in temperature, the G band position reaches 1590 cm^{-1} suggesting the formation of a nanocrystalline graphitic phase above 400 °C. A similar trend in the peak position is observed for the D band (Figure 11b). It starts at 1344 cm^{-1} and steeply increases toward 1358 cm^{-1}, followed by a further linear shift, reaching 1372 cm^{-1} at 450 °C, indicating clustering and ordering of the crystallites as discussed earlier.

Interestingly, a similar trend in G band position is observed in case of carbon lines annealed at different temperatures (Figure 12a). It can be seen that the G band position starts at 1564 cm^{-1} (higher than for dots) and continues to shift up to 1576 cm^{-1} at 150 °C followed by a small plateau region between 150 and 250 °C. Further increase in the annealing temperature above 250 °C leads to the formation of a graphitic phase as indicated by the G band position reaching 1580 cm^{-1}. Yet, even further increase in the temperature leads to the nucleation of nanocrystalline domains implying the formation of nanocrystalline graphite as can be concluded from band shift above 1590 cm^{-1}. Correspondingly, the D band position follows similar trend with increasing annealing temperature, further implying the formation of a more ordered graphitic phase (Figure 12b).

Overall, a continuous increase in the G band and D band positions with increasing annealing temperature strongly supports the argument made above about the formation of nanocrystalline graphitic carbon domains based upon the morphological changes and D/G analysis. The slight decrease in the G band and D band peak position near 450 °C is difficult to validate by the experimental measurements. However, it might suggest the disruption of the nanocrystalline domains caused by the process of ablation at the highest temperature exploited here.

GENERAL DISCUSSION AND CONCLUSIONS

Thus, our study demonstrates that three distinct structural transformations take place inside the carbon EBID deposits during annealing within a temperature range from 100 to 450 °C as presented in Figures 10 and 11. These transformations involves loss of adsorbed/absorbed moisture around 100 °C, dehydrogenation and stress relaxation at temperatures within 100−200 °C, followed by the intense graphitization and the formation of nanocrystalline graphitized nanostructures at the annealing temperatures, above 350 °C. By comparing these thermally induced transformations in the nanoscale EBID deposits with those typically observed for the bulk amorphous carbon films, one can conclude that generally, they follow known transformation for bulk carbon materials except for several significant features as mentioned below.

First, dehydration and dehydrogenation occurs at lower annealing temperatures (100−200 °C) which significantly affect the physical state of nanoscale deposits. Second, at relatively low temperatures, within 150−250 °C, nanoscale carbon deposits undergo significant stress relaxation, (usually not observed for bulk materials) owing to the significant confinement effects resulting from the large contribution of surface and interfacial regions. Finally, increase in annealing temperature leads to the similar transformations for both carbon dots and lines but it tends to be more gradual in carbon lines as compared to the dots. This difference further supports the argument that the heat transfer process occurs more efficiently in the lines than the dots owing to their higher interfacial area with the metal underneath. It is worth noting that overall trends in phase transformation of carbon deposits stay unchanged for different volumes over 4 orders of magnitude ranging from few cubic micrometers for the largest line down to 1×10^{-3} μm^3 for the smallest dot.

Considering the fact that electronic devices generally fabricated at relatively low temperatures to avoid any thermal effects to adversely affect the properties of the device components. Thus, in order to use these materials for electronic device applications, it is critically important that ultimate phase transformations for carbon deposits occur at much lower annealing temperatures (300−350 °C) than the bulk materials. This difference makes EBID carbon deposits more attractive than those prepared by different methods such as physical vapor deposition, chemical vapor deposition and sputtering.

Indeed, for these carbon materials complete graphitization and formation of nanocrystalline carbon occurs at significantly lower temperatures than that observed for amorphous carbon films (600−800 °C).[16,39] We suggest that this significant difference is caused by the fact that the specific surface area for the nanoscale deposits is significantly larger than that for the bulk films, with annealing at ambient conditions also contributing. Moreover, the presence of a heterogeneous interface along with significant surface phonon vibrations on a nanoscale largely influence the physical and chemical properties of the material.[46,47] Moreover, EBID carbon differs from these commonly used techniques primarily in terms of its physical composition and structure by having imbedded volatile species (hydrogen and CH_x). Thus, upon annealing the EBID deposits and the resulting ablation, the formation of a porous structure might occur from the release of hydrogen and other embedded volatile species in contrast with traditional carbon films. Such porous structure may further collapse resulting in post-thermal-processing volume, which is much smaller than that based on just change in density of graphite vs amorphous carbon.

Finally, as we suggested in the beginning, these nanoscale carbon deposits might be exploited for making carbon−metal interconnect elements of future microdevices. The results of our study suggest that modest thermal annealing can dramatically increase conductivity of these deposits due to its intense graphitization, important for establishing a robust interconnect. However, the size of the deposits limits the use of most characterization methods for simple measurements of the conductivity of these nanostructures. Studies are ongoing to address this issue in near future by using conductive atomic force microscopy[49] but it is a very challenging study that will be discussed separately.

In summary, the shape of the deposits and interfacial areas play an important role in the phase transformation behavior of amorphous nanoscale EBID carbon and needs to be considered for its prospective applications in high-performance multifunctional devices. In fact, the ability to graphitize nanoscale amorphous carbon deposits at much lower temperatures compatible with fabrication and packaging microelectronic process allows to effectively control the microstructure of the deposits for creating highly conductive ohmic interconnects across heterogeneous junctions. This further facilitates the need to produce the localized annealing of the nanosize deposits, which will be the focus of our future studies.

EXPERIMENTAL SECTION

Fabrication of EBID Carbon Deposits. Residual hydrocarbons and acetone was used as a precursor molecule to induce the growth of the deposits over clean Au/Cr substrates. EBID carbon joints are fabricated using Quanta 200 ESEM operated under 0.01 Pa. The cone-shaped carbon deposits shown in Figure 1 were deposited by keeping the electron beam in spot mode for a period of 20 min. Electron beam energy in 10 to 30 keV range and electron beam current (spot size) in the 5−140 pA range was used for deposition. The carbon dots shown in Figure 3 were are made by scanning the electron beam at energy of 25 keV and current of ∼20 pA at a frame time of 0.411s and resolution of 2048 × 1768 pixels for a period varying from 5 to 240 s. The carbon lines shown in Figure 4 were deposited under line mode with similar SEM settings by varying the exposure time from 30 s to 20 min. These deposits were annealed under atmospheric conditions at different temperatures for 3 min.

Characterization Methods. AFM images were collected using a Dimension-3000 microscope using silicon tips with tip radii between 10 and 20 nm and a spring constant of about 40 N/m in accordance with usual procedure established in our group.[48,49] The samples were scanned at 0.5−0.7 Hz. The domain height and surface area coverage for the lines and dots were determined from cross-sectional and bearing analysis, respectively.

Raman data was obtained using a WITec (Alpha 300R) confocal Raman microscope using Ar+ ion laser (514.5 nm) as an excitation source.[43] The images were obtained by scanning an area of 30 μm × 10 μm for the lines and 24 μm × 8 μm for the dots with a 50× objective (Olympus 50X-NA = 0.75). The spectra were obtained under minimum laser power (0.5 mW) to avoid any laser induced annealing as was verified independently. The integration time was optimized at 1 s for the deposits in Figure 2 and 2 s for the deposits in Figures 3 and 4 in order to obtain higher signal-to-noise ratio. The spectra were integrated between 1000 and 1800 cm^{-1} to account for the D band and G band. A grating with 600 grooves/mm grating having a spectral resolution of 4 cm^{-1} was used for this study.

AUTHOR INFORMATION

Corresponding Author
*E-mail: vladimir@mse.gatech.edu.

ACKNOWLEDGMENT

Semiconductor Research Corporation (GRC Grant 2008OJ1864.1281) and NSF Grant CBET-0930781 provided financial support for this work.

REFERENCES

(1) Silva, S. R. P. *Properties of Amorphous Carbon*; INSPEC; Institution of Engineering and Technology: Herts, U.K., 2003.
(2) Zhang, P.; Tay, B. K.; Sun, C. Q.; Lau, S. P. *J. Vac. Sci. Technol., A* **2002**, *20*, 1390–1394.
(3) Beghi, M. G.; Ferrari, A. C.; Teo, K. B. K.; Robertson, J.; Botani, C. E.; Libassi, A.; Tanner, B. K. *Appl. Phys. Lett.* **2002**, *81*, 3804–3806.
(4) Bull, S. J. *Diamond Relat. Mater.* **1995**, *4*, 827–836.
(5) Choi, W. S.; Hong, B. *Renewable Energy* **2008**, *33*, 226–231.
(6) Zhang, W.; Catherine, Y. *Surf. Coat. Technol.* **1991**, *47*, 69–83.
(7) Rother, B.; Siegel, J.; Breuer, K.; Muhling, I.; Deutschmann, S.; Vetter, J.; Trommer, G.; Rau, B.; Heiser, C. *J. Mater. Res.* **1991**, *6*, 101–111.
(8) Voevdin, A. A.; Donley, M. S. *Surf. Coat. Technol.* **1996**, *82*, 199–213.
(9) Onoprienko, A. A.; Yanchuk, I. B. *Powder Metall. Met. Ceram.* **2006**, *45*, 190–195.
(10) Robertson, J. *J. Mater. Sci. Eng. R.* **2002**, *37*, 129–281.
(11) Rossi, F.; Andre, B.; Veen, A. V.; Mijnarends, P. E.; Schut, H.; Delplanke, M. P.; Gissler, W.; Haupt, J.; Lucazeau, G.; Abello, L. *J. Appl. Phys.* **1994**, *75*, 3121–3129.
(12) Urso, L. D.; Compagnini, G.; Puglisi, O. *Carbon* **2006**, *44*, 2096–2098.
(13) Chu, P. K.; Li, L. *Mater. Chem. Phys.* **2006**, *96*, 253–277.
(14) Onodera, A.; Irie, Y.; Higashi, K.; Umermeura, J.; Takenaka, T. *J. Appl. Phys.* **1991**, *69*, 2611–2617.
(15) Schwan, J.; Ulrich, S.; Batori, V.; Ehrardt, H.; Silva, S. R. P. *J. Appl. Phys.* **1996**, *80*, 440–447.
(16) Reinke, P.; Oelhafen, P. *J. Appl. Phys.* **1997**, *81*, 2396–2399.
(17) Raravikar, N. R.; Keblinski, P.; Rao, A. M.; Dresselhaus, M. S.; Schadler, L. S.; Ajayan, P. M. *Phys. Rev. B.* **2002**, *66*, 235424–1−235424−9.
(18) Jiang, C.; Ko, H.; Tsukruk, V. V. *Adv. Mater.* **2005**, *17*, 2127–2131.

(19) Ko, H.; Pikus, Y.; Jiang, C.; Jauss, A.; Hollricher, O.; Tsukruk, V. V. *Appl. Phys. Lett.* **2004**, *85*, 2598–2600.
(20) Wang, Y.; Alsmeyer, D. C.; McCreery, R. L. *Chem. Mater.* **1990**, *2*, 557–563.
(21) Nemanich, R. J.; Solin, S. A. *Phys. Rev. B* **1981**, *20*, 392–401.
(22) Ferrari, A. C.; Robertson, J. *Phys. Rev. B* **2000**, *61*, 14095–14107.
(23) Tuinstra, F.; Koenig, J. L. J. *Chem. Phys.* **1970**, *53*, 1126–1130.
(24) Ferrari, A. C.; Robertson, J. *Philos. Trans. R. Soc. London, Ser. A* **2004**, *362*, 2477–2512.
(25) Kelly, B. T. *Physics of Graphite*; Applied Science Publishers: London, 1993.
(26) Koidl, P.; Wagner, C.; Dischler, B.; Wagner, J.; Ramsteiner, M. *Mater. Sci. Forum* **1990**, *52*, 41.
(27) Hart, R. K.; Kassner, T. F.; Maurin, J. K. *Philos. Mag.* **1970**, *21*, 453–467.
(28) Rykaczewski, K.; White, W. B.; Fedorov, A. G. *J. Appl. Phys.* **2007**, *101*, 054307–1.
(29) Rykaczewski, K.; Marshall, A.; White, W. B.; Fedorov, A. G. *Ultramicroscopy* **2008**, *108*, 989–992.
(30) Banhart, F. *Nano Lett.* **2001**, *1*, 329–332.
(31) Rykaczewski, K.; Hilderth, O. J.; Kulkarni, D. D.; Henry, M. R.; Kim, S. -K; Wong, C. P; Tsukruk, V. V.; Fedorov, A. G. *ACS Appl. Mater. Interfaces* **2010**, *2*, 969–975.
(32) Guan, Y.; Fowlkes, J. D.; Retterer, S. T.; Simpson, M. L.; Rack, P. D. *Nanotechnology* **2008**, *19*, 505302.
(33) Ding, W.; Dikin, D. A.; Chen, X.; Piner, R. D.; Ruoff, R. S.; Zussman, E.; Wang, X.; Li., X. *J. Appl. Phys.* **2005**, *98*, 014905–1.
(34) Rykaczewski, K.; Henry, M. R.; Kim, S. -K.; Fedorov, A. G.; Kulkarni, D. D.; Singamaneni, S.; Tsukruk, V. V. *Nanotechnology* **2010**, *21*, 035202.
(35) Marchon, B.; Heiman, N.; Khan, M. R.; Lautie, A.; Ager, J. W.; Veirs, D. K. *J. Appl. Phys.* **1991**, *69*, 5748–5750.
(36) Onodera, A.; Yasushi, I.; Higashim, K.; Umemura, J.; Takenaka, T. *J. Appl. Phys.* **1991**, *69*, 043512–1.
(37) Mounier, E.; Bertin, F.; Adamik, M.; Pauleau, Y.; Barna, P. B. *Diamone Relat. Mater.* **1996**, *5*, 1509–1515.
(38) Cho., N. H.; Veirs, D. K.; Ager, J. W.; Rubin, M. D.; Hopper, C. B.; Bogy, D. B. *J. Appl. Phys.* **1992**, *71*, 2243–2248.
(39) Jiu, J. T.; Wang, H.; Cao, C.-B.; Zhu, H. S. *J. Mater. Sci.* **1999**, *34*, 5205–5209.
(40) Takabayashi, S.; Okamoto, K.; Sakaue, H.; Takahagi, T.; Shimada, K.; Nakatani, T. *J. Appl. Phys.* **2008**, *104*, 043512.
(41) Walters, J. K.; Fox, D. M.; Burke, T. M.; Weedon, O. D.; Newport, R. J.; Howells, W. S. *J. Chem. Phys.* **1994**, *101*, 4288–4300.
(42) Osswald, S.; Yushin, G.; Mochalin, V.; Kucheyev, S. O.; Gogotsi, Y. *J. Am. Chem. Soc.* **2006**, *128*, 11635–11642.
(43) Singamaneni, S.; Gupta, M. K.; Yang, R.; Tomczak, M.; Naik, R. R.; Wang, Z. L.; Tsukruk, V. V. *ACS Nano* **2009**, *3*, 2593.
(44) Kuptsov, A. H.; Zhizhin, G. N. *Handbook of Fourier Transform Raman and Infrared Spectra of Polymers*; Elsevier: New York, 1998.
(45) Sullivan, J. P.; Friedmann, T. A.; Baca, A. G. *J. Electron. Mater.* **1997**, *26*, 1021–1029.
(46) Buffat., P. H.; Borel, J.-P. *Phys. Rev. A* **1976**, *13*, 2287–2298.
(47) Shi, F. G. *J. Mater. Res.* **1994**, *9*, 1307–1313.
(48) Tsukruk, V. V. *Rubber Chem. Technol.* **1997**, *70*, 430.
(49) McConney, M. E.; Singamaneni, S.; Tsukruk, V. V. *Polym. Rev.* **2010**, *50*, 235–286.